This is a postprint version of the following published document:

Peñas-López, P., van Elburg, B., Parrales, M. A. & Rodríguez-Rodríguez, J. (2017). Diffusion of dissolved CO_2 in water propagating from a cylindrical bubble in a horizontal Hele-Shaw cell. *Phys. Rev. Fluids* 2, 063602.

DOI: 10.1103/PhysRevFluids.2.063602

Diffusion of dissolved CO₂ in water propagating from a cylindrical bubble in a horizontal Hele-Shaw cell

Pablo Peñas-López,[*] Benjamin van Elburg, Miguel A. Parrales, and Javier Rodríguez-Rodríguez

Fluids Mechanics Group, Universidad Carlos III de Madrid, Avda. de la Universidad 30, 28911, Leganés (Madrid), Spain

The dissolution of a gas bubble in a confined geometry is a problem of interest in technological applications such as microfluidics or carbon sequestration, as well as in many natural flows of interest in geophysics. While the dissolution of spherical or sessile bubbles has received considerable attention in the literature, the case of a two-dimensional bubble in a Hele-Shaw cell, which constitutes perhaps the simplest possible confined configuration, has been comparatively less studied. Here, we use planar laser-induced fluorescence to experimentally investigate the diffusion-driven transport of dissolved CO_2 that propagates from a cylindrical mm-sized bubble in air-saturated water confined in a horizontal Hele-Shaw cell. We observe that the radial trajectory of an isoconcentration front, $r_f(t)$, evolves in time as approximately $r_f - R_0 \propto \sqrt{t}$, where R_0 denotes the initial bubble radius. We then characterize the unsteady CO_2 concentration field via two simple analytical models, which are then validated against a numerical simulation. The first model treats the bubble as an instantaneous line source of CO_2, whereas the second assumes a constant interfacial concentration. Finally, we provide an analogous Epstein-Plesset equation with the intent of predicting the dissolution rate of a cylindrical bubble.

I. INTRODUCTION

Gas-liquid mass transfer is a vital phenomenon in many environmental issues (waste water treatment, gas absorption in oceans [1], CO_2 sequestration [2], etc.), and in industrial applications (bubble columns, bioreactors [3], etc.). Moreover, gas exchange with bubbles in confinement is of common occurrence in microfluidics [4,5].

Planar laser-induced fluorescence (PLIF) is a widely used nonintrusive technique for the two-dimensional visualization of dissolved gas transport in aqueous flows [6]. PLIF has enabled the study of mass transport across free and wind-forced interfaces [7–10], wakes of rising bubbles [11–15], and bubbly swarms [16]. The emission intensity of some fluorescent dyes such as rhodamine is inhibited by oxygen quenching. This provides a fast and effective way of measuring O_2 concentrations and diffusivity in liquids [10,15]. Similarly, other dyes are sensitive to pH. Such is the case of sodium fluorescein, whose emission intensity increases nonlinearly with pH in the range ∼3−9 [17]. pH-sensitive LIF is a useful method to quantify CO_2 absorption in liquids [9,14], and it can be likewise employed as a means to accurately measure the diffusivity of CO_2 in water [18]. In a recent work, Vreme *et al.* [19] made use of it to visualize the gravitational (convective) instability triggered by the dissolution of carbon dioxide through a water-gas interface in a vertical Hele-Shaw cell.

Strictly diffusion-driven concentration fields evolving from strictly planar interfaces are given by the well-known one-dimensional error-function profile. These profiles have been verified through LIF experiments, whence the diffusivity of gases in liquids could be measured through experimental fitting [10,18]. Similarly, much effort has gone into the modeling of the diffusion-driven dissolution or growth of spherical bubbles. The solution provided by Epstein and Plesset [20] is highly popular
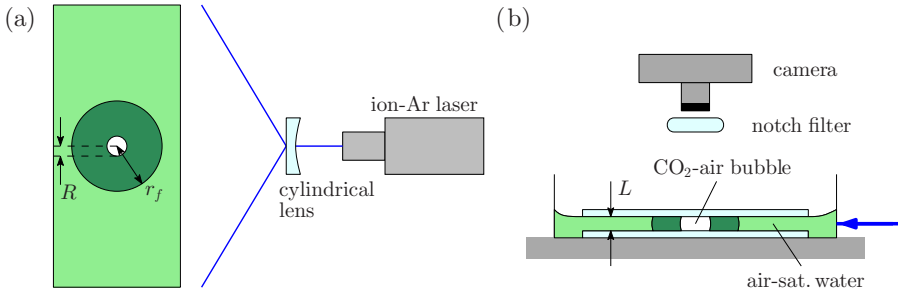
FIG. 1. (a) Plan view and (b) side view of the experimental setup. PLIF reveals a CO_2-containing region [dark green region enclosed by $r_f(t)$] propagating radially outward from the dissolving cylindrical bubble of radius $R(t)$.

and yields quite good agreement with dissolution experiments concerning monocomponent [21] and multicomponent bubbles [22].

Cylindrical (pancake-shaped) bubbles can be easily found inside rectangular channels in microfluidic environments. Several studies have focused on the cavitation [23] and pulsation dynamics [24] of such bubbles. For this configuration, however, the phenomenon of diffusion-driven gas transfer has not been given much attention, to the best of our knowledge, despite its interest in modern microfluidic applications. In such configurations, confinement introduces additional length scales (the thickness of the channel) and a contact-angle dynamics that in principle may introduce differences with the dissolution dynamics expected for an ideal two-dimensional bubble. Such behaviors, for instance, have been recently observed for the dissolution of sessile droplets in microchannels by Bansal and co-workers [25].

Thus, with the idea of assessing to what extent a pancake confined bubble may be modeled as a two-dimensional one, in this work we investigate via pH-sensitive PLIF the fundamental problem consisting in the radial diffusion of dissolved CO_2 in air-saturated water propagating from a mm-sized cylindrical bubble in a horizontal Hele-Shaw cell. By means of experiment, simulation, and approximate analytical models, we characterize (i) the behavior of the propagating CO_2-rich boundary layer and (ii) the bubble dissolution dynamics. Another question of interest that we address in this work is whether the dissolution dynamics of a two-dimensional bubble can be described, even in an approximate way, by an equation similar to that of Epstein-Plesset, which strictly speaking does not exist for a cylindrical bubble due to the lack of an analytical solution for the concentration field.

Finally, we would like to mention that the relative simplicity of the experimental setup, and the fact that visualization of the phenomenon can be achieved to a decent degree by a scattered UV light source rather than a laser sheet, implies that this experiment possibly embodies a canonical demonstration of diffusion-driven mass transfer in liquids, suitable for undergraduate and even high-school courses.

II. EXPERIMENTS

The experimental setup in Fig. 1 comprises a horizontally oriented Hele-Shaw cell composed of two 2.4×6 cm^2 plain glass microscope slides separated by a gap of width $L = 1$ mm. The cell is filled with air-saturated distilled water containing fluorescein sodium dye ($\sim 10^{-7}$ mol/L). A continuous ion-argon laser (Stabilite 2017, Spectra-Physics) operating at 488 nm produces a horizontal laser sheet that penetrates along the gap of the cell. A bubble containing a CO_2-air mixture is then injected manually (at time $t = 0$) by means of a syringe. The bubble injection and dissolution process are recorded from above. Images are acquired at 0.5 fps for around 40 min by an iPhone 5 camera operated through the commercial application Lapse It Pro. The camera is placed behind a 488 nm notch filter (Thorlabs) to isolate the recorded fluorescence from any unwanted laser reflections.
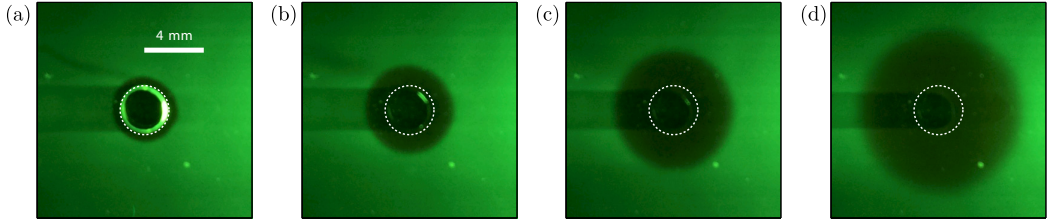
FIG. 2. Raw PLIF snapshots of the bubble surrounded by a propagating CO_2 front taken at (a) $t = 10$ s, (b) $t = 1$ min, (c) $t = 3$ min, and (d) $t = 8$ min after bubble injection. The dotted white circle marks the initial perimeter of the dissolving bubble. The horizontal dark slab left of the bubble is the bubble shadow. These snapshots correspond to the experiment with initial CO_2 fraction $X_0 = 0.55$ (see Fig. 3).

The emission intensity of fluorescein is known to be inhibited by decreasing pH and hence increasing CO_2 concentration. Consequently, as sketched in Fig. 1 and now seen in Fig. 2, PLIF images reveal a dark (CO_2-containing) circular region propagating radially outward from the bubble into a brighter (CO_2-free) region.

Six individual experiments were performed on different days. The precise composition of the CO_2-air mixture contained in the syringe at the time of injection bubble is unknown and it is expected to be different for each experiment. This is because, as the syringe was filled, some CO_2 gas unavoidably escaped and got replaced by air from the environment.

The time evolution of the bubble radius, $R(t)$, is plotted in Fig. 3. The experimental bubble radii were obtained through averaged measurements of the divergent shade thickness of the bubble across a strip close to the bubble surface. The net shrinkage of the bubbles is attributed to the diffusion-driven exchange of CO_2 gas and air across the bubble interface. More specifically, a prominent outflow of CO_2 gas into the liquid and a lesser inflow of air into the bubble take place simultaneously. The higher solubility of CO_2 with respect to that of air ultimately accounts for the significant difference in magnitude of the fluxes. A quasistable bubble radius is achieved when the bubble is almost depleted of CO_2. Thereafter, the bubble is practically entirely composed of air. Note that a very small flux of CO_2 continues to be expelled from the bubble, resulting in a slow but still observable bubble dissolution rate.
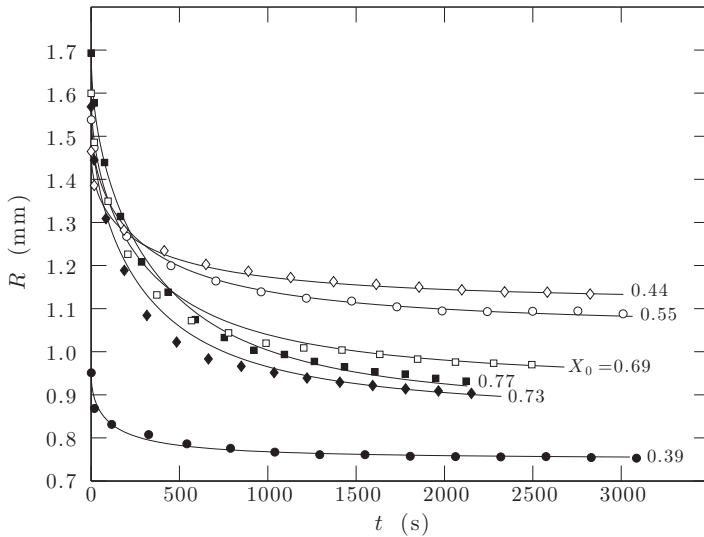

FIG. 3. Evolution of the bubble radius with time for six different experiments, each possessing a distinctive initial mole fraction of CO_2, X_0. Experiments (markers) are compared with simulation (solid lines).

3

The smooth evolution of $R(t)$ hints that contact line dynamics are not inherently important on the dissolution process since no sudden jump or stick events are observed. This implies that the bubble retains an almost cylindrical shape throughout the recorded dissolution process. Moreover, no detachment from the lower plate is observed during the experiments. This stands to reason since the contact angle is expected to be close to $90°$, even for bigger gap thicknesses (see Fig. 14). The quasiequilibrium radius of the bubble is hence sufficiently large for detachment not to occur. Of course, for full dissolution events or for slender pillar-shaped bubbles with small radius to height ratios, detachment from the lower plate is certain to occur. This would result in a spherical cap bubble that remains adhered to the top plate.

To clearly identify each experiment, the experiments are tagged by the initial mole fraction of CO_2, X_0, a free parameter determined from simulation. The simulation solves the advection-diffusion equation for two gas species: CO_2 and air, assuming that the liquid is initially perfectly saturated with air and has zero CO_2 concentration. This allows us to properly quantify the air desorption into the bubble and CO_2 dissolution into the water. In addition, these mass transport equations are coupled with the mass conservation equations for both species across the bubble interface so as to obtain the radius dynamics $R(t)$. The full problem is derived in Appendix A, and essentially consists in the discretization and numerical integration of the PDE system presented in Eqs. (A7) and (A8). Throughout this paper, we have used the label "simulation" to refer to the complete solution obtained in this way. Later on, the solutions obtained from the simulation will also act as a reference with which to compare approximate analytical diffusion models describing the evolution of the concentration field (Sec. III) in addition to an Epstein-Plesset-type model describing the dissolution dynamics (Sec. IV).

A. Image processing

The raw RGB images were converted to grayscale intensity images by taking just the green channel. An image processing algorithm inspired by the one employed by Dani *et al.* [11] was implemented to compensate for the long-term fluctuations of the laser power and the spatial inhomogeneity of the lighting. Let $0 \leqslant G_m(x,y,t) \leqslant 1$ denote the measured grayscale value of a pixel with coordinates (x,y) of a raw grayscale image taken at time t. Then,

$$G(x,y,t) = 1 - \left[G_{\text{ref},m}(x,y) - G_m(x,y,t)\frac{I_{\text{ref}}}{I(t)} \right] \tag{1}$$

is the corrected grayscale value of such a pixel. $G_{\text{ref},m}(x,y)$ denotes the measured grayscale value of the pixel in the reference image. The first image acquired immediately after bubble injection was chosen as the reference image. Lastly, I_{ref} is the mean intensity registered on a selected rectangular portion of the reference image, while $I(t)$ is the analogous intensity associated with the image taken at time t. Figure 4 compares a raw LIF image with its processed counterpart.

Since the diffusion process is, in principle, radially symmetric, it is reasonable to quantify the evolution of the CO_2 field by computing the radial intensity profile $\overline{G}(r,t)$ from the processed images. $\overline{G}(r,t)$ is defined as the averaged value of $G(x,y,t)$ along a circumference located at a radial distance r from the (immobile) bubble center. Such a profile is plotted at different times in Fig. 5. The profile clearly behaves in a way one would expect for a diffusion-driven scalar such as concentration. Close to the bubble surface there is a high level of disturbance in $\overline{G}$ due to light reflections [13], as one may infer from Fig. 2(a). Note that this region has been removed in Fig. 5.

B. Objectives

A quantity of interest is the radius of the boundary-layer leading edge, that is, the apparent boundary-layer thickness of the radial CO_2 concentration field optically perceived by PLIF that, hereafter, will be referred to as "front." The snapshots in Fig. 2 suggest that it is possible to quantify the highly visible edge of the boundary layer.
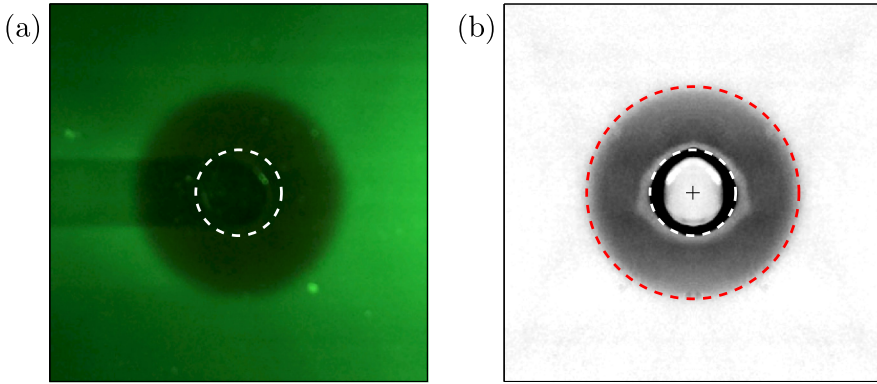
FIG. 4. Comparison of (a) a raw image and (b) a processed image. The white dotted circle marks the initial bubble circumference, while the red dotted circle marks the front position at which $\overline{G} = 0.9$.

We have defined the term "front" as the leading edge of the boundary layer. More specifically, it can be regarded as the isoconcentration contour $C(r_f, t) = C_f$, corresponding to a constant value in intensity, $\overline{G}(r_f, t) \sim 0.85\text{--}0.95$, where $r_f(t)$ denotes the radial trajectory of the front. The processed snapshot in Fig. 4 verifies that this intensity range reasonably marks the position of the front.

Figures 6(a) and 6(b) plot the front trajectories in dimensional and dimensionless form, respectively, at which $\overline{G} = 0.9$. R_0 denotes the initial bubble radius, and we employ $D = 1.89 \times 10^{-9}$ m^2/s as the diffusivity of CO_2 in water. The error bars indicate the thickness of the front spanned by the intensity range 0.85–0.95.

The dispersion between the different curves observed in Fig. 6(b) is a consequence of the fact that the gray level intensity, G_m, could not be calibrated as a function of the pH (or conversely CO_2 concentration), due to the limitations of our experimental system. Consequently, the value of the CO_2 concentration at the front differs between different experiments. Nonetheless, this paper focuses on physical aspects of the dynamics of the concentration field that will be shown not to depend on its precise value at the front. More specifically, the next section will aim at exploring two questions:

(i) What are the front trajectory dynamics? Do the fronts propagate as $\sqrt{t}$ like those evolving from a planar interface? This is not immediately obvious since, even neglecting the effect of gravity, there is one additional length scale in the problem, namely the bubble radius $R(t)$. Thus, when the size
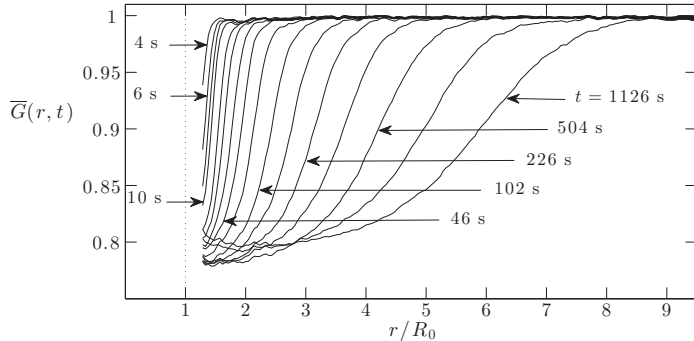

FIG. 5. Evolution in time of the radial intensity profile corresponding to the experiment with $X_0 = 0.39$. The profile is plotted at several log-spaced times after bubble injection. R_0 (in the abscissa label) denotes the initial bubble radius.
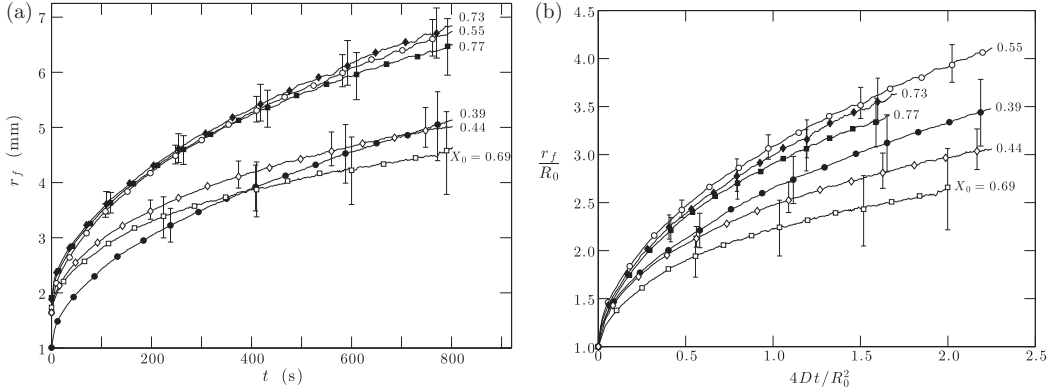
FIG. 6. (a) Front radial trajectories corresponding to $\overline{G} = 0.9$ for the six experiments. Upper and lower values of the error bars mark the front radii corresponding to $\overline{G} = 0.95$ and 0.85, respectively. (b) Same front trajectories plotted in dimensionless form.

of the concentration boundary layer is of the order of $R(t)$, one may in principle expect a departure from this power law.

(ii) How does the corrected intensity profile relate to the concentration and pH profiles?

III. FRONT PROPAGATION AND CONCENTRATION PROFILES

A. Formulation and nondimensionalization

Let us consider a cylindrical bubble of radius R confined in a horizontal Hele-Shaw cell of constant thickness L. The bubble dissolution rate is assumed sufficiently small to dismiss the effect of inertia, viscosity, and interface-induced advection. Moreover, the gap thickness L is sufficiently thin to neglect the effect of gravity and natural convection.

The mass transport equation for the dissolved CO_2 gas in water is then well approximated by the diffusion equation in cylindrical coordinates with radial symmetry and no axial dependence,

$$\frac{\partial C}{\partial t} = \frac{D}{r} \frac{\partial}{\partial r} \left(r \frac{\partial C}{\partial r} \right). \tag{2}$$

Here, C is the molar-based concentration of dissolved CO_2 gas in the liquid. The boundary and initial conditions read

$$C(R,t) = C_s(t), \tag{3a}$$

$$C(\infty,t) = C(r > R,0) = C_\infty = 0. \tag{3b}$$

In our case there is no CO_2 gas initially dissolved in the liquid. In this section, we shall take advantage of the fact that $C_\infty = 0$ to simplify the formulation.

Note that the full problem additionally requires a joint mass conservation equation for the CO_2 and air species in order to simultaneously determine $R(t)$ and the interfacial concentrations that serve as boundary conditions to the (advection)-diffusion equation for both CO_2 and air. The full problem, whose solution is referred to as "simulation," is synthesized (in dimensionless form) in Eqs. (A7) and (A8) in Appendix A. Nonetheless, it will be shown that, to a first approximation, the spatiotemporal evolution of the CO_2 concentration field can be reasonably well reproduced by simple diffusion models that do not consider the effect of bubble shrinkage or the exact variation of $C_s(t)$, as if the total gas mass was released instantaneously at the origin. In such a case, one final

6

quantity is required, namely

$$C_{b,0} = \frac{X_0 P_\infty}{R_u T_\infty},\tag{4}$$

the initial (partial) CO_2 concentration inside the bubble. R_u denotes the universal gas constant, while P_∞ and T_∞ refer to the ambient (and bubble) pressure and temperature. Let us nondimensionalize the radial coordinate and time as follows:

$$\xi = \frac{r}{R_0},\tag{5a}$$

$$\tau = \frac{4D}{R_0^2}t.\tag{5b}$$

We may then define the dimensionless CO_2 concentration u as a fraction of $C_{b,0}$, in addition to the dimensionless concentration c as a fraction of the saturation concentration,

$$u(\xi,\tau) = \frac{C(r,t)}{C_{b,0}},\tag{6a}$$

$$c(\xi,\tau) = \frac{C(r,t)}{k_H P_\infty},\tag{6b}$$

where $k_H = 3.4 \times 10^{-4}$ mol/m^3 Pa is Henry's coefficient. The concentrations are related through $c = X_0 u/\Lambda$, where $\Lambda = k_H R_u T_\infty$ is the CO_2 solubility parameter. It represents the ratio of the interfacial CO_2 concentration to the partial CO_2 concentration inside the bubble. Finally, the dimensionless front can be written as $u_f = u(\xi_f,\tau)$ or $c_f = c(\xi_f,\tau)$.

B. Front trajectory and concentration

There exists no analytical solution in terms of standard functions for $C(r,t)$ to Eqs. (2) and (3), even when approximating $R(t)$ and $C_s(t)$ as constants. As a fast alternative to solving the full problem numerically, it is reasonable to model the mass transport problem as an instantaneous line source (ILS) of CO_2 deposited at some negative time $-t_s$ to account for the fact that mass is being released from the finite bubble boundary at $r = R(t)$ and that the initial bubble radius is finite, $R_0 > 0$. Moreover, this time shift, or virtual time origin, t_s, also accounts for the fact that the bubble shrinkage period is not instantaneous. The duration of the period of initial development enters at long times as a shift in the time coordinate, needed to improve the accuracy of the long-time description given here. Virtual origins are commonly used in boundary-layer analyses to improve the far-field description of spatially developing flows, as was done by Revuelta *et al.* [26] for the submerged jet. These authors showed, by means of a rigorous perturbative analysis of the point-source solution, that this virtual origin is in fact the first-order correction to the leading-order description in the limit of large distances. A similar perturbative analysis, employing the rescaled time as an asymptotically large quantity, can be employed for the bubble evolution analyzed here to show that the concentration field described by the ILS model is the leading-order result.

With these ideas in mind, one must then solve (2) together with the initial condition

$$C(r,-t_s) = \pi R_0^2 C_{b,0}\, \delta(r),\tag{7}$$

where $t_s > 0$ is a time-shift constant and $\delta(r)$ is the Dirac delta. The well-known solution reads [27]

$$C(r,t) = \frac{\pi R_0^2 C_{b,0}}{4\pi D(t + t_s)} \exp\left(-\frac{r^2}{4D(t + t_s)}\right).\tag{8}$$

Modeling this problem as an ILS of dissolved mass can be justified when it concerns a highly soluble gas. In such a case, the most important parameter that influences $C(r,t)$ is the total mass of gas to be
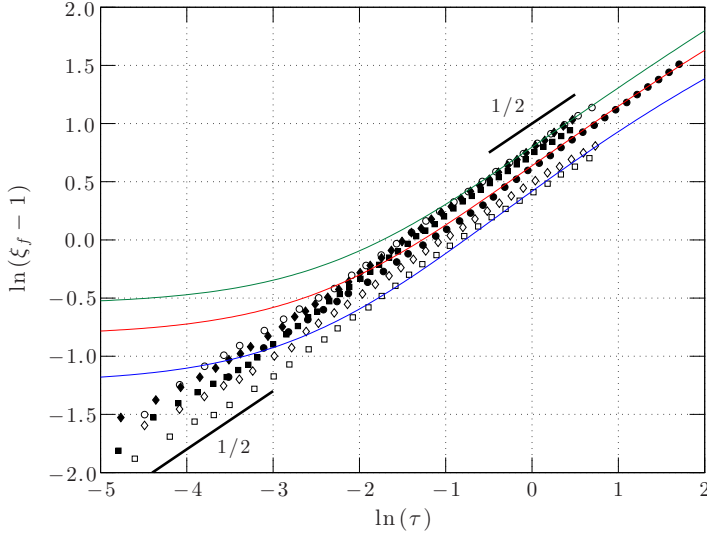
FIG. 7. Experimental front trajectories (markers) corresponding to $\overline{G} = 0.95$. ILS diffusion model curves given by Eq. (10) are drawn with $\tau_s = 0.25$ and $u_f = 0.02\%$ (upper curve), 0.1% (middle) and 0.5% (lower).

released by the bubble. This quantity is quite insensitive to the bubble shrinkage $R(t)$ or interfacial concentration $C_s(t)$. It eventually overrides the effect of $R(t)$ and $C_s(t)$ on the concentration field $C(r,t)$ that would be observed at a distance sufficiently away from the bubble. Of course, at small times, $C(r,t)$ is confined to a small region close to the bubble and it greatly depends on said effects—one cannot simply ignore the existence of the bubble. We remark that at small times and at $r \approx R_0$, the ILS model is not suitable, and consequently its solution is not expected to be valid.

Next, let us neatly simplify Eq. (8) to

$$u(\xi,\tau) = \frac{1}{\tau + \tau_s} \exp\left\{-\frac{\xi^2}{\tau + \tau_s}\right\} \tag{9}$$

by rewriting it in dimensionless form. Rearranging (9) yields an expression for the front trajectory:

$$\xi_f^2(\tau) = -(\tau + \tau_s)\ln\{(\tau + \tau_s)u_f\}. \tag{10}$$

We must stress again that the expressions for concentration profiles $u(\xi,\tau)$ written in Eq. (9) and trajectories $\xi_f(\tau)$ in Eq. (10) are not valid when evaluated at the spatiotemporal region close the bubble interface (where ξ or $\xi_f \approx 1$). This statement holds true regardless of the τ_s chosen. Note that at short times after the bubble injection, the ILS diffusion model fails since the front trajectories of interest are indeed very close to the bubble interface.

However, an appropriate value for τ_s will improve the accuracy of the model in its potential range of validity. The time shift t_s must be proportional to the time required for diffusion to act over distance R_0. Since $R_0 \sim \sqrt{Dt_s}$, then $\tau_s = 4Dt_s/R_0^2$ is expected to remain fairly constant for all experiments. As shown next, the value $\tau_s \approx 0.25$ was determined from the experimental trajectories.

To do so, first we subtracted R_0 from the experimental front trajectories and plotted the result in logarithmic form. This is presented in Fig. 7. Remarkably, the experimental points fall on an approximately straight curve of slope $1/2$. This is not immediately obvious for the cylindrical geometry due to the existence of an additional length scale R_0. Thus, to a good approximation, the front trajectory obeys $r_f - R_0 \propto \sqrt{Dt}$ (or $\xi_f - 1 \propto \sqrt{\tau}$ in dimensionless form). The modeled trajectory, Eq. (10), is also plotted for three different values of the front concentration u_f (free

parameter). The ILS diffusion model predicts well the front trajectory except, as expected, at very short times after bubble injection. The experimental early-time slope of $1/2$ observed can be justified by the thin boundary-layer approximation in which the concentration field essentially sees the bubble interface as a constant-concentration planar boundary. On the other hand, at longer times, namely for $\ln \tau > -1$ (where $\tau > 0.37$ and $\xi_f > 2$), the ILS diffusion model fully captures the asymptotic $\xi_f - 1 \propto \sqrt{\tau}$ behavior. We conclude that this is precisely the region in which the the ILS model is potentially valid.

Mathematically, it can be verified that the slope of the curves of the ILS diffusion model plotted in Fig. 7, namely

$$\frac{d \ln (\xi_f - 1)}{d \ln \tau} = \frac{1}{2} \frac{\xi_f(\tau)}{\xi_f(\tau) - 1} \frac{\tau}{\tau + \tau_s} \left[1 - \frac{\tau + \tau_s}{\xi_f^2(\tau)} \right], \tag{11}$$

asymptotically tends to $1/2$ as $\tau \to \infty$ and $\xi_f \to \infty$. Note that the term in square brackets in Eq. (11) tends to unity. This can be seen by rewriting it as $1 - 1/\ln\{(\tau + \tau_s)u_f\}$ by means of (10). Setting the left-hand side of (11) equal to $1/2$ at $\tau \approx 1$, where $\xi_f \sim 2$–3 according to Fig. 6(b), one gets $\tau_s \sim 0.3$. It then follows from (10) that u_f must be of the order of 0.01–1 % of $C_{b,0}$.

In the intermediate stage, once the boundary layer $r_f - R_0$ becomes comparable to R_0 [when $\ln(\xi_f - 1) \approx -1$], we can notice the effect of the length scale R_0: the slope of the front trajectories increases slightly beyond $1/2$. Nonetheless, the deviation from the continuous $1/2$ slope is, to a reasonable degree, negligible.

In the spirit of the result that approximately $\xi_f - 1 \propto \sqrt{\tau}$, we now show that it is also possible to describe the diffusion problem by means of a constant interface concentration (CIC) diffusion model. We assume a negligible change in bubble radius, $R \approx R_0$, and we fix the interfacial CO_2 concentration at a mean value: $C(R_0,t) = X_0 k_H P_\infty/2$ (note that the Laplace pressure is neglected). Even with these approximate boundary conditions, an exact solution based on the similarity variable $\eta = (r - R_0)/\sqrt{4Dt}$ does not exist for the cylindrical geometry, as opposed to the planar geometry, with solution $C(r,t) \propto \mathrm{erfc}(\eta)$, or the spherical geometry, where $C(r,t) \propto \mathrm{erfc}(\eta)/r$. Nonetheless, an approximate solution, formally valid for small times ($\tau \lesssim 1$), is derived in Appendix B. It reads

$$\frac{C(r,t)}{X_0 k_H P_\infty/2} = \sqrt{\frac{R_0}{r}} \mathrm{erfc} \left(\frac{r - R_0}{\sqrt{4Dt}} \right). \tag{12}$$

Straightforward manipulation of (12) yields an implicit expression for the dimensionless front trajectory,

$$(\xi_f - 1)/\mathrm{erfc}^{-1} \left(\frac{2u_f \sqrt{\xi_f}}{\Lambda} \right) = \sqrt{\tau}. \tag{13}$$

Figure 8 shows the front trajectories from three different experiments according to the ILS and CIC diffusion models, in addition to those obtained from our numerical simulation (see Appendix A). The simulation dictates the front concentration value u_f that is then used by both models. Overall a fair agreement is observed.

C. Intensity, concentration, and pH profiles

We shall proceed to address the second question posed in Sec. II B: what is the relationship between intensity and pH/concentration? Before doing so, we must first obtain the pH from C, the dissolved CO_2 gas concentration in mol/L, by [3]

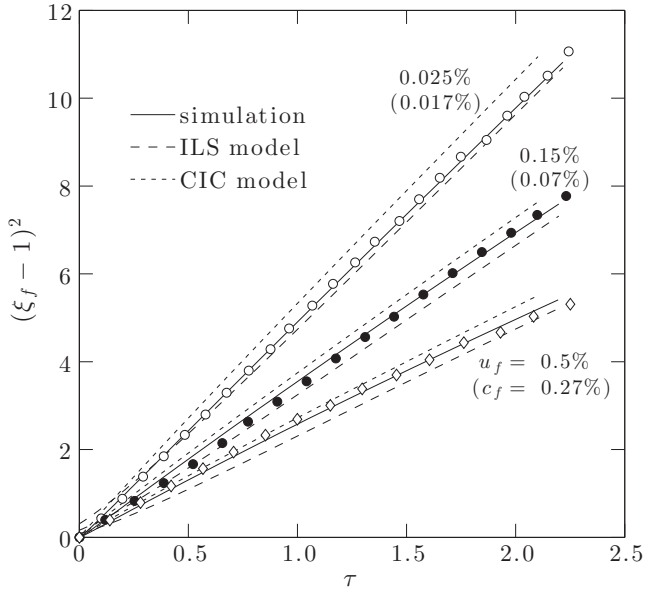$$\mathrm{pH} = -\log_{10} \sqrt{K_w + K_a C}, \tag{14}$$

FIG. 8. Experimental front trajectories (markers) corresponding to $\overline{G} = 0.95$ labeled with the predicted front concentration u_f (c_f) according to simulation. Simulation, ILS model (10) and CIC model (13) trajectories are also shown.

where $K_w = 10^{-14}$ is the self-ionization constant of water, and $K_a = 4.4 \times 10^{-7}$ is the acidity constant of dissolved carbon dioxide (usually quoted as the dissociation constant of carbonic acid).

The concentration/pH profiles obtained from the ILS model are then validated against simulation. The profiles for the experiment with $X_0 = 0.39$ are shown in Figs. 9 and 10 at four different time instants. The agreement between the ILS model and simulation improves as τ increases, as seen in Fig. 9. The corrected intensity $\overline{G}$ has also been plotted in Figs. 9 and 10 assuming that $\overline{G}$ varies linearly with concentration (their changes are thus proportional, $\Delta \overline{G} \propto \Delta C$) and alternatively, assuming that $\overline{G}$ varies linearly with pH ($\Delta \overline{G} \propto \Delta$pH).

Under the assumption that $\Delta \overline{G} \propto \Delta C$, we have computed the concentration as $C = A_1(1 - \overline{G})$, with $A_1 = 4.76 \times 10^{-4}$ mol/L so that $c_f = 0.07\%$ falls on $\overline{G} = 0.95$ as predicted by simulation (note that its trajectory is plotted in Fig. 8). Similarly, for $\Delta \overline{G} \propto \Delta$pH, we compute the pH from $7 - \text{pH} = A_2(1 - \overline{G})$, where $A_2 = 11.5$ is a fitting parameter.

For the smallest concentrations corresponding to a pH level above 5.3, i.e., at the leading edge of the boundary layer ($\overline{G} > 0.85$), the relation $\Delta \overline{G} \propto \Delta C$ holds. Thus, in this region, we observe a Stern-Volmer-type relationship [11,14] that is typically applied to describe fluorescence quenching by oxygen [7,10]. On the other hand, for lower values of pH, $\overline{G}$ is observed to change fairly linearly with pH, a result that was reported by Asher and Litchendorf [9] for a similar range in pH. In any case, the nonlinear relationship between fluorescence of sodium fluorescein and pH or concentration [17] is corroborated.

IV. BUBBLE DISSOLUTION MODEL

The theory developed by Epstein and Plesset [20] provides a simple yet effective model that describes the growth or dissolution of stationary, spherical bubbles. Whereas in Sec. III B we modeled the concentration field neglecting the effect of bubble shrinkage, we now focus on describing the other part of the picture: the bubble radius dynamics $R(t)$. Toward that end, the mass conservation
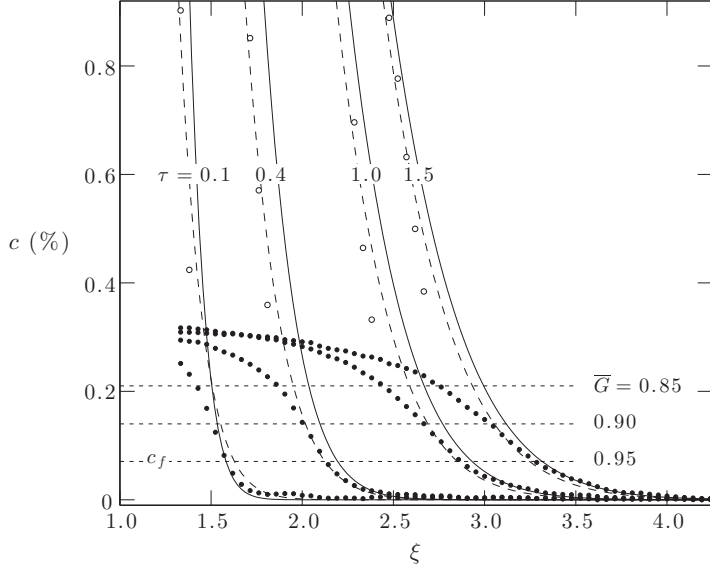
FIG. 9. Concentration profiles according to—simulation and - - - the ILS model. The corrected intensity $\overline{G}$ is plotted assuming that (•) $\Delta\overline{G} \propto \Delta C$ or (○) $\Delta\overline{G} \propto \Delta\text{pH}$.

equation across the bubble interface must be directly implemented. The purpose here is to derive an analogous expression to the Epstein-Plesset equation adapted to the cylindrical geometry as an alternative to the complete numerical simulation. Let us consider the "quasistationary" concentration field $C(r,t)$ that would evolve from a static cylindrical bubble of radius R and constant interfacial concentration C_s. An approximate solution for $C(r,t)$, formally valid for small times, is found in Eq. (B3) in Appendix B. Likewise, the interfacial gradient can be expressed in terms of a constant
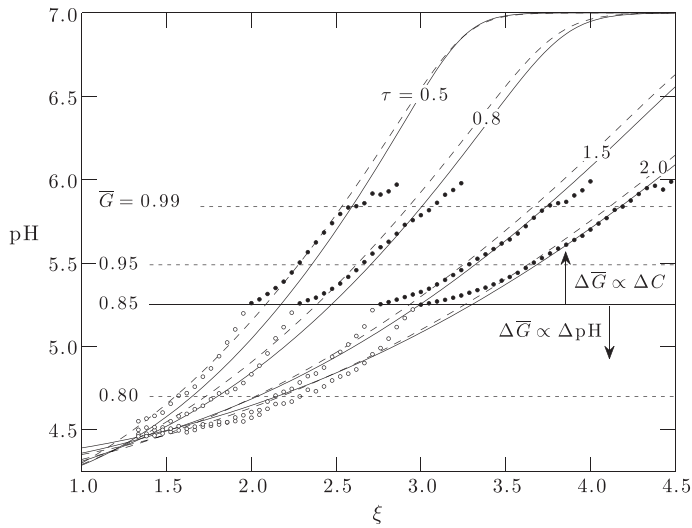

FIG. 10. pH profiles from - - - the ILS model and—simulation. The corrected intensity $\overline{G}$ is plotted assuming that (•) $\Delta\overline{G} \propto \Delta C$ or (○) $\Delta\overline{G} \propto \Delta\text{pH}$.
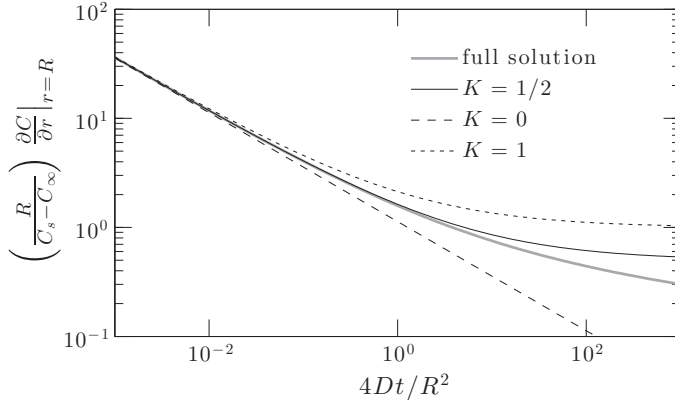
11

FIG. 11. Time history of the concentration gradient at a stationary cylindrical, planar, and spherical interface.

geometry factor, K, as follows:

$$\frac{\partial C}{\partial r}\bigg|_{r=R} = -(C_s - C_\infty)\left[\frac{1}{\sqrt{\pi D t}} + \frac{K}{R}\right]. \tag{15}$$

As shown in Appendix B, we obtain $K = 1/2$ using the methods of Laplace transforms and substitution. As seen in Fig. 11, the approximate analytical solution taking Eq. (15) with $K = 1/2$ deviates from the exact solution (B11) only at long times. For comparison, the interfacial concentration gradient of a planar interface ($K = 0$) and a spherical bubble of radius R ($K = 1$) [20] are also shown.

An important limitation of our upcoming model is that we assume the bubble retains a cylindrical shape at all times. Thus, the bubble volume and surface area change according to $\pi R^2(t)L$ and $2\pi R(t)L$, respectively. This is unrealistic in full dissolution events or in initially slender, pillar-shaped bubbles where contact line dynamics and detachment eventually become important.

Making use of Fick's first law and the ideal gas equation of state, the molar flow rate across a monocomponent gas bubble is known to satisfy

$$\frac{d}{dt}\left(\frac{P_\infty \pi L}{R_u T_\infty}R^2(t)\right) = 2\pi R(t)LD\frac{\partial C}{\partial r}\bigg|_{r=R}. \tag{16}$$

Note that surface tension is neglected since for the relatively large pancake bubbles considered here ($R \sim 1$ mm), the Laplace pressure is expected to be small. Combining (15) and (16), we find that the rate of change of the bubble radius of a cylindrical bubble immersed in a liquid-gas solution of uniform (molar-based) concentration C_∞ is given by the following analogous Epstein-Plesset equation:

$$\frac{dR}{dt} = -\frac{D R_u T_\infty}{P_\infty}(C_s - C_\infty)\left[\frac{1}{\sqrt{\pi D t}} + \frac{K}{R}\right], \tag{17}$$

where $C_s = k_H P_\infty$. Figure 12 compares the dissolution dynamics of a monogas bubble according to our model and numerical simulation. Note that these curves are independent of the initial bubble size R_0. For the case of a CO_2 bubble, shown in Fig. 12(a), the dissolution rate is noticeably slower than that predicted by the quasistationary model with the exact interfacial gradient. This is attributed to the shell effect: an expansion of the boundary layer due to advection. Note that advection is taken into account in the simulation, whereas it has been inherently neglected in all forms of the quasistationary model. Naturally, for slow dissolution rates the effect of advection is negligible. Consequently, for the slowly dissolving air bubble portrayed in Fig. 12(b), both solutions behave identically.
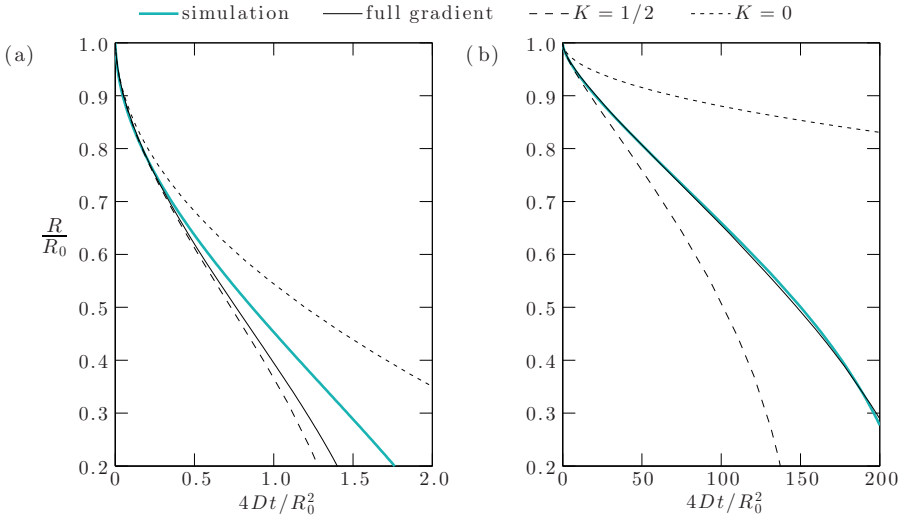
FIG. 12. Dissolution dynamics of a cylindrical bubble under ambient conditions in degassed water. The curves correspond to a bubble entirely composed of (a) CO_2 gas (high solubility) and (b) air (poor solubility). We show the solutions according to our numerical simulation (cf. Appendix A) and quasistationary model with the full interfacial gradient (numerically computed) given by Eqs. (16) and (B11). We also plot the solutions of our simplified quasistationary model in Eq. (17) setting $K = 1/2$ (short-time approximation) and $K = 0$ (planar interface).

Moreover, it stands to reason that the quasistationary model based on the short-time analytical solution ($K = 1/2$) performs well during fast dissolution events, as seen in Fig. 12(a). However, as one may observe in Fig. 12(b), it overestimates the mass flux at longer times. This is consistent with the results shown in Fig. 11. Finally, it is verified that for monogas bubble dissolution, the dissolution rate is broadly underestimated when a planar interface ($K = 0$) is assumed.

The extension of the quasistationary model to deal with multicomponent gas bubbles is straightforward. This has been done in Refs. [22,28,29] for the case of spherical (cap) bubbles. The interfacial concentration of the ith species is proportional to the partial pressure of the gas, $C_{s,i}(t) = k_{H,i} P_\infty X_i$, while the corresponding molar number is $n_i = \pi R_0^2 L P_\infty X_i / (R_u T_\infty)$. For a system comprising N gas species, we need to integrate a system of $N + 1$ ODEs,

$$\frac{dR}{dt} = -\frac{R_u T_\infty}{P_\infty} \sum_{i=1}^{N} D_i [C_{s,i}(t) - C_{\infty,i}] \left[\frac{1}{\sqrt{\pi D_i t}} + \frac{K}{R(t)} \right],$$

$$\frac{dn_i}{dt} = -2\pi R L D_i [C_{s,i}(t) - C_{\infty,i}] \left[\frac{1}{\sqrt{\pi D_i t}} + \frac{K}{R(t)} \right], \quad i = 1, \dots, N, \tag{18}$$

subject to the initial radius R_0 and molar fractions $X_{i,0}$.

This model is compared against simulation in Fig. 13 for different values of the initial CO_2 molar fraction, X_0. Under the experimental conditions considered here, the agreement is surprisingly better when assuming a planar interface. In such a case, the (negative) error in the interfacial mass flux is compensated by the (positive) error arising from the (advectionless) quasistationary approximation. Apart from the effect of advection, the (positive) error is mainly attributed to the extension of the quasistationary approximation to the interfacial concentrations of the species, since these are treated as constant in the obtention of the expression for the concentration gradient [28]. In other words, the error comes from not taking into account the so-called history effect [30,31]. The history effect
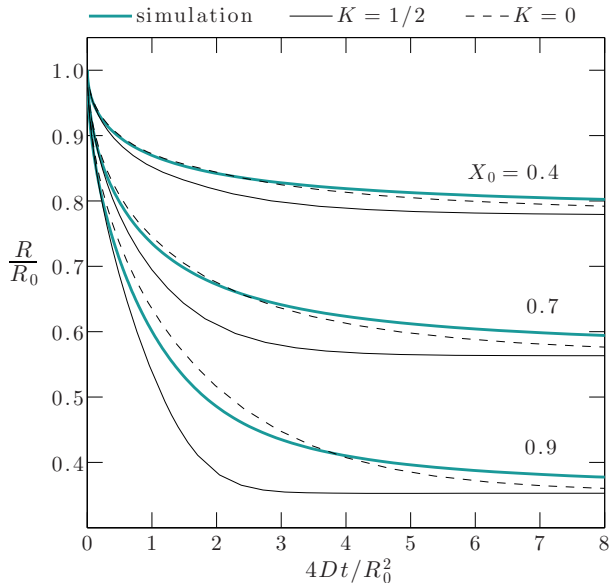
13

FIG. 13. Dissolution dynamics of a CO_2-air cylindrical bubble in air-saturated water according to our numerical simulation and our quasistationary model in Eq. (18) upon the assumption of a circular ($K = 1/2$) or planar ($K = 0$) interface.

can be summarized as the contribution of the preceding time history of the interfacial concentration on the current rate of growth or dissolution. For multicomponent bubbles, the variation in time of the species interfacial concentration, $C_{s,i}(t)$, is usually inevitable. As recently shown by Chu and Prosperetti [31], the history effect can be taken into account by the inclusion of a computationally costly history integral term in all the ODEs in Eq. (18).

V. CONCLUDING REMARKS

The boundary layer of dissolved CO_2 propagating by diffusion from a cylindrical bubble in air-saturated water confined in a horizontal Hele-Shaw cell has been experimentally visualized by means of PLIF. The trajectories of the leading-edge isoconcentration fronts have been shown to evolve as $r_f - R_0 \propto \sqrt{Dt}$, with little dependence on the value of the front concentration. The
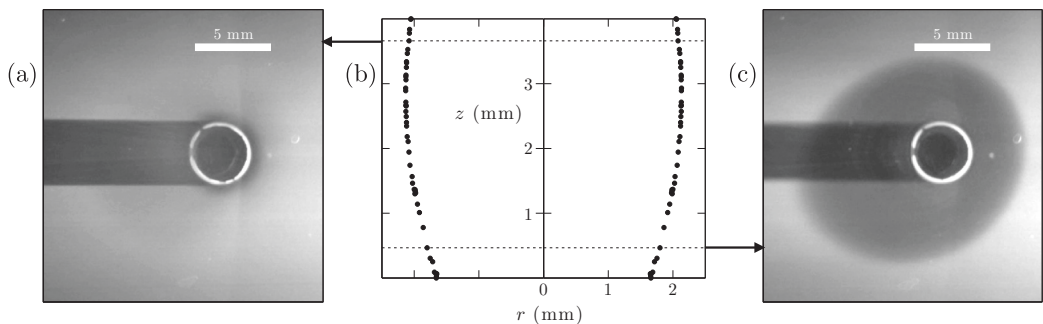

FIG. 14. Large gap thickness ($L = 4$ mm) experiment 3 min after bubble injection. Two snapshots reveal the CO_2 boundary layer observed (plan view) when the laser sheet penetrates the cell (a) close to the top glass slide and (c) close to the bottom slide. Panel (b) shows the cross section of the bubble at that time.

14

diffusion-driven transport of CO_2 is described by two simple analytical diffusion models. The first is based on an instantaneous line source, whereas the second assumes a constant interfacial concentration. These are then validated against numerical simulation, which solves the full problem regarding a dissolving multicomponent bubble. Lastly, we derive an analogous Epstein-Plesset equation that is able to effectively predict the bubble dissolution rate.

A final remark is that gravitational effects such as density-induced natural convection have been neglected throughout this work. This is reasonable since the cell is kept in a horizontal position. However, the onset of convection is bound to appear after some time for inclinations as small as $0.1°$ [32]. The onset time and strength of the convective instability is governed by the Rayleigh number. In our problem, it represents the ratio of the radial pressure gradient arising from a horizontal density (CO_2 concentration) gradient and the opposing viscous force. Simple dimensional analysis shows that the Rayleigh number scales with L^3. Thus, for large cell thickness, the convection-driven regime dominates. This is corroborated in an experiment where the thickness is increased fourfold to $L = 4$ mm. As portrayed in Fig. 14, a purely height-independent diffusion-driven regime is no longer observed. Instead, the denser CO_2-rich fluid immediately sinks to the bottom, spreading as a dense gravity current [33].

ACKNOWLEDGMENTS

APPENDIX A: FULL PROBLEM FORMULATION FOR THE NUMERICAL SIMULATION

The transport equation for the ith gas species may be approximated as the advection-diffusion equation in cylindrical coordinates with radial symmetry,

$$\frac{\partial C_i}{\partial t} + \frac{\dot{R}R}{r}\frac{\partial C_i}{\partial r} = \frac{D_i}{r}\frac{\partial}{\partial r}\left(r\frac{\partial C_i}{\partial r}\right), \tag{A1}$$

where $C_i(r,t)$ is the molar concentration of species i, while $D_i(r,t)$ denotes the mass diffusivity. We have made the approximation that at the bubble interface, $r = R(t)$, the (vertically averaged) radial velocity is simply $\langle u_r(R,t)\rangle = \dot{R}$. Thus, from continuity, it follows that $\langle u_r(r,t)\rangle = \dot{R}R/r$. Note that the averaged velocity satisfies the Hele-Shaw equation $\langle u_r\rangle = L^2/(12\mu)\,\partial p/\partial r$.

The usual boundary and initial conditions for the concentration apply,

$$C_i(R,t) = C_{s,i} = k_{H,i}P_\infty n_i/n, \tag{A2a}$$

$$C_i(\infty,t) = C_i(r > R,0) = C_{\infty,i}. \tag{A2b}$$

Symbol $k_{H,i}$ refers to Henry's coefficient; $n_i(t)$ is the number of moles of gas i inside the bubble, whereas $n(t)$ is the sum of $n_i(t)$ over all species. Note that surface tension is neglected, so the bubble pressure is assumed equal to the ambient pressure, P_∞. This system is most easily solved in dimensionless form. Toward that end, let us introduce

$$\tau = \frac{4D_1}{R_0^2}t, \tag{A3a}$$

$$\xi = \frac{r}{R(t)} \tag{A3b}$$

as the dimensionless time and radial coordinate, where R_0 is the initial bubble radius. Note that this definition for ξ differs from the definition given in Eq. (5a), which is then used throughout the main sections of the paper. The advantage of letting $\xi = r/R(t)$ here is that the nonstationary cylindrical

interface of the bubble remains fixed at $\xi = 1$ always. The dimensionless concentration field

$$c_i(\xi,\tau) = \frac{C_i(r,t) - C_{\infty,i}}{k_{H,i} P_\infty} \tag{A4}$$

and normalized mole number of the sum over all species

$$\mu(\tau) = \sum_{i=1}^{N} \mu_i(\tau) = \sum_{i=1}^{N} \frac{R_u T_\infty}{\pi L R_0^2 P_\infty} n_i(t) \tag{A5}$$

are the solution quantities of interest. Assuming that the bubble remains cylindrical at all times, the dimensionless radius, $a = R/R_0$, is related to the dimensionless mole number simply by the ideal gas law: $a^2 = \mu$. Finally, let us define the far-field saturation parameter, solubility parameter, and diffusivity ratio:

$$\Upsilon_i = \frac{C_{\infty,i}}{k_{H,i} P_\infty}, \tag{A6a}$$

$$\Lambda_i = k_{H,i} R_u T_\infty, \tag{A6b}$$

$$\Gamma_i = D_i/D_1. \tag{A6c}$$

The dimensionless rate of molar transfer is given by mass conservation,

$$\frac{d\mu}{d\tau} = \sum_{i=1}^{N} \frac{d\mu_i}{d\tau} = \sum_{i=1}^{N} \frac{1}{2} \Gamma_i \Lambda_i \left. \frac{\partial c_i}{\partial \xi} \right|_{\xi=1}. \tag{A7}$$

Finally, the dimensionless form of the mass transport equation (A1) for every species becomes

$$\frac{\partial c_i}{\partial \tau} = \frac{\Gamma_i}{4\mu} \frac{\partial^2 c_i}{\partial \xi^2} + \frac{1}{4\mu} \left[\Gamma_i + 2(\xi^2 - 1) \frac{d\mu}{d\tau} \right] \frac{1}{\xi} \frac{\partial c_i}{\partial \xi} \tag{A8}$$

subject to $c_i(1,\tau) = \mu_i/\mu - \Upsilon_i$ and $c_i(\infty,\tau) = 0$.

The known initial conditions at $\tau = 0$ are $c_i(\xi > 1, 0) = 0$, $\mu_{i,0} = X_{0,i}$, where $X_{0,i}$ is the initial mole fraction inside the freshly injected bubble. Taking species $i = 1$ to be CO_2 and $i = 2$ to be air, we set $\Upsilon_1 = 0$ and $\Upsilon_2 = 1$. We then numerically integrate (A7) and (A8) in τ to find the primary solution variables c_i, μ_i. Equation (A8) is spatially discretized using a centered, second-order finite-difference scheme. Numerical infinity is taken at $\xi = 15$.

APPENDIX B: ANALYTICAL TREATMENT OF THE CYLINDRICAL DIFFUSION EQUATION

Here we proceed to present a solution, formally valid for small times, to the diffusion equation (2) subject to the boundary conditions in Eq. (3). A cylindrical bubble of fixed radius R is considered. Moreover, the interfacial concentration C_s is assumed constant over time.

The substitution variable

$$w(r,t) = \sqrt{r} \, \frac{C(r,t) - C_\infty}{C_s - C_\infty} \tag{B1}$$

transforms (2) to a planar diffusion equation with a source term,

$$\frac{\partial w}{\partial t} = D \frac{\partial^2 w}{\partial r^2} + \frac{Dw}{4r^2}, \tag{B2}$$

subject to $w(R,t) = \sqrt{R}$ and $w(\infty,t) = w(r,0) = 0$. The characteristic length scale in the derivatives, ∂r, is of the order of the boundary-layer thickness, which evolves as $\sqrt{4Dt}$. The characteristic length scale of the source term is $r \sim R$. A simple magnitude balance between the last

two terms reveals that the source term can be neglected if $\partial r^2 \ll 4r^2$. This is true for small times, i.e., when $Dt \ll R^2$, i.e., $\tau \ll 1$. Omitting the source term, the solution reads

$$\frac{C(r,t) - C_\infty}{C_s - C_\infty} = \sqrt{\frac{R}{r}} \ \text{erfc}\left(\frac{r - R}{\sqrt{4Dt}}\right) \tag{B3}$$

and the interfacial concentration gradient is given by

$$\left.\frac{\partial C}{\partial r}\right|_{r=R} = -(C_s - C_\infty)\left[\frac{1}{\sqrt{\pi Dt}} + \frac{1}{2R}\right]. \tag{B4}$$

Solutions (B3) and (B4) can be verified through the Laplace transform method and asymptotic expansion for short times. It is convenient to first nondimensionalize the variables as

$$c(\xi,\tau) = \frac{C(r,t) - C_\infty}{C_s - C_\infty}, \tag{B5a}$$

$$\xi = \frac{r}{R}, \tag{B5b}$$

$$\tau = \frac{Dt}{R^2}. \tag{B5c}$$

Equation (2) becomes

$$\frac{\partial c}{\partial \tau} = \frac{1}{\xi}\frac{\partial}{\partial \xi}\left(\xi\frac{\partial c}{\partial \xi}\right), \tag{B6}$$

with $c(1,\tau) = 1$ and $c(\infty,\tau) = 0$. Taking then the Laplace transform of (B6) subject to the initial condition $c(\xi,0) = 0$ results in a modified Bessel differential equation

$$\xi^2\frac{d^2\hat{c}}{d\xi^2} + \xi\frac{d\hat{c}}{d\xi} - s\xi^2\hat{c} = 0, \tag{B7}$$

with $\hat{c}(1;s) = 1/s$ and $\hat{c}(\infty;s) = 0$. The solution for the transformed concentration field, compatible with our boundary conditions, reads

$$\hat{c}(\xi;s) = \frac{1}{s}\frac{K_0(\sqrt{s}\xi)}{K_0(\sqrt{s})}, \tag{B8}$$

where K_0 is the zeroth-order modified Bessel function of the second kind. The asymptotic behavior of $\hat{c}$ for small times ($\tau \to 0$) is

$$\lim_{s\to\infty}\hat{c}(\xi;s) = e^{-\sqrt{s}(\xi-1)}\left[\frac{1}{s\sqrt{\xi}} + O(s^{-3/2})\right]. \tag{B9}$$

Likewise, the transformed interfacial gradient behaves as

$$\lim_{s\to\infty}\left\{\left.\frac{\partial\hat{c}}{\partial\xi}\right|_{\xi=1}\right\} = \lim_{s\to\infty}\left\{-\frac{1}{\sqrt{s}}\frac{K_1(\sqrt{s})}{K_0(\sqrt{s})}\right\} = -\left[\frac{1}{\sqrt{s}} + \frac{1}{2s} + O(s^{-3/2})\right]. \tag{B10}$$

Antitransforming (B9) and (B10) naturally renders solutions (B3) and (B4). Moreover, the exact solution for the interfacial concentration gradient can be numerically determined by first applying an inversion algorithm [34] on

$$\left.\frac{\partial C}{\partial r}\right|_{r=R} = -(C_s - C_\infty)\frac{R}{D}\ \mathcal{L}^{-1}\left\{\frac{1}{R\sqrt{s/D}}\frac{K_1(R\sqrt{s/D})}{K_0(R\sqrt{s/D})}\right\}(t). \tag{B11}$$

[1] B. Jähne and H. Haußecker, Air-water gas exchange, Annu. Rev. Fluid Mech. **30**, 443 (1998).

[2] H. E. Huppert and J. A. Neufeld, The fluid mechanics of carbon dioxide sequestration, Annu. Rev. Fluid Mech. **46**, 255 (2014).

[3] A.-J. Mäki, M. Peltokangas, J. Kreutzer, S. Auvinen, and P. Kallio, Modeling carbon dioxide transport in PDMS-based microfluidic cell culture devices, Chem. Eng. Sci. **137**, 515 (2015).

[4] R. Sun and T. Cubaud, Dissolution of carbon dioxide bubbles and microfluidic multiphase flows, Lab Chip **11**, 2924 (2011).

[5] A. Volk, M. Rossi, C. J. Kähler, S. Hilgenfeldt, and A. Marín, Growth control of sessile microbubbles in PDMS devices, Lab Chip **15**, 4607 (2015).

[6] J. P. Crimaldi, Planar laser induced fluorescence in aqueous flows, Exp. Fluids **44**, 851 (2008).

[7] H. Herlina and G. H. Jirka, Application of LIF to investigate gas transfer near the air-water interface in a grid-stirred tank, Exp. Fluids **37**, 341 (2004).

[8] J. W. Walker and W. L. Peirson, Measurement of gas transfer across wind-forced wavy air-water interfaces using laser-induced fluorescence, Exp. Fluids **44**, 249 (2008).

[9] W. E. Asher and T. M. Litchendorf, Visualizing near-surface concentration fluctuations using laser-induced fluorescence, Exp. Fluids **46**, 243 (2009).

[10] M. Jimenez, N. Dietrich, A. Cockx, and G. Hébrard, Experimental study of O_2 diffusion coefficient measurement at a planar gas-liquid interface by planar laser-induced fluorescence with inhibition, AIChE J. **59**, 325 (2013).

[11] A. Dani, P. Guiraud, and A. Cockx, Local measurement of oxygen transfer around a single bubble by planar laser-induced fluorescence, Chem. Eng. Sci. **62**, 7245 (2007).

[12] M. Stöhr, J. Schanze, and A. Khalili, Visualization of gas-liquid mass transfer and wake structure of rising bubbles using pH-sensitive PLIF, Exp. Fluids **47**, 135 (2009).

[13] J. Francois, N. Dietrich, P. Guiraud, and A. Cockx, Direct measurement of mass transfer around a single bubble by micro-PLIFI, Chem. Eng. Sci. **66**, 3328 (2011).

[14] P. Valiorgue, N. Souzy, M. E. Hajem, H. B. Hadid, and S. Simoëns, Concentration measurement in the wake of a free rising bubble using planar laser-induced fluorescence (PLIF) with a calibration taking into account fluorescence extinction variations, Exp. Fluids **54**, 1501 (2013).

[15] N. Dietrich, J. Francois, M. Jimenez, A. Cockx, P. Guiraud, and G. Hébrard, Fast measurements of the gas-liquid diffusion coefficient in the gaussian wake of a spherical bubble, Chem. Eng. Technol. **38**, 941 (2015).

[16] E. Alméras, S. Cazin, V. Roig, F. Risso, F. Augier, and C. Plais, Time-resolved measurement of concentration fluctuations in a confined bubbly flow by LIF, Int. J. Multiphase Flow **83**, 153 (2016).

[17] D. A. Walker, A fluorescence technique for measurement of concentration in mixing liquids, J. Phys. E **20**, 217 (1987).

[18] A. Sell, H. Fadaei, M. Kim, and D. Sinton, Measurement of CO_2 diffusivity for carbon sequestration: A microfluidic approach for reservoir-specific analysis, Environ. Sci. Technol. **47**, 71 (2013).

[19] A. Vreme, F. Nadal, B. Pouligny, P. Jeandet, G. Liger-Belair, and P. Meunier, Gravitational instability due to the dissolution of carbon dioxide in a Hele-Shaw cell, Phys. Rev. Fluids **1**, 064301 (2016).

[20] P. S. Epstein and M. S. Plesset, On the stability of gas bubbles in liquid-gas solutions, J. Chem. Phys. **18**, 1505 (1950).

[21] G. Kapodistrias and P. H. Dahl, Scattering measurements from a dissolving bubble, J. Acoust. Soc. Am. **131**, 4243 (2012).

[22] S. Shim, J. Wan, S. Hilgenfeldt, P. D. Panchal, and H. A. Stone, Dissolution without disappearing: Multicomponent gas exchange for CO_2 bubbles in a microfluidic channel, Lab Chip **14**, 2428 (2014).

[23] E. Zwaan, S. Le Gac, K. Tsuji, and C.-D. Ohl, Controlled Cavitation in Microfluidic Systems, Phys. Rev. Lett. **98**, 254501 (2007).

[24] Y. A. Ilinskii, E. A. Zabolotskaya, T. A. Hay, and M. F. Hamilton, Models of cylindrical bubble pulsation, J. Acoust. Soc. Am. **132**, 1346 (2012).

[25] L. Bansal, S. Chakraborty, and S. Basu, Confinement-induced alterations in the evaporation dynamics of sessile droplets, Soft Matter **13**, 969 (2017).

[26] A. Revuelta, A. L. Sánchez, and A. Liñán, The virtual origin as a first-order correction to the far-field description of laminar jets, Phys. Fluids **14**, 1821 (2002).

[27] J. Crank, in *The Mathematics of Diffusion*, 2nd ed. (Clarendon, Oxford, 1975), Chap. 3, p. 28.

[28] M. C. Weinberg and R. S. Subramanian, Dissolution of multicomponent bubbles, J. Am. Ceram. Soc. **63**, 527 (1980).

[29] P. Peñas-López, M. A. Parrales, and J. Rodríguez-Rodríguez, Dissolution of a CO_2 spherical cap bubble adhered to a flat surface in air-saturated water, J. Fluid Mech. **775**, 53 (2015).

[30] P. Peñas-López, M. A. Parrales, J. Rodríguez-Rodríguez, and D. van der Meer, The history effect in bubble growth and dissolution. Part 1. Theory, J. Fluid Mech. **800**, 180 (2016).

[31] S. Chu and A. Prosperetti, History effects on the gas exchange between a bubble and a liquid, Phys. Rev. Fluids **1**, 064202 (2016).

[32] A. C. Slim, M. M. Bandi, J. C. Miller, and L. Mahadevan, Dissolution-driven convection in a Hele-Shaw cell, Phys. Fluids **25**, 024101 (2013).

[33] C. W. MacMinn, J. A. Neufeld, M. A. Hesse, and H. E. Huppert, Spreading and convective dissolution of carbon dioxide in vertically confined, horizontal aquifers, Water Resour. Res. **48**, W11516 (2012).

[34] J. Abate and W. Whitt, A unified framework for numerically inverting Laplace transforms, INFORMS J. Comput. **18**, 408 (2006).